Ionic Liquid Mixture at the Vacuum Interface and the Peaks and Antipeaks Analysis of X-ray Reflectivity

Fei Wu, Waruni V. Karunaratne, and Claudio J. Margulis*

Department of Chemistry, University of Iowa, Iowa City, Iowa 52242, United States

E-mail: claudio-margulis@uiowa.edu

Abstract

This article presents work on the structure of the ionic liquid mixture between 1-Methyl-3-octylimidazolium Octylsulfate and 1-Ethyl-3-methylimidazolium Ethylsulfate at the vacuum interface. In particular, we focus on the relative concentration of components as a function of distance to the interface and the formation of a nanoscopic apolar blocking layer that encloses a second thicker and much more polar interfacial layer. We present a thorough analysis of the time scale for convergence of structural features as they dissipate into the bulk and provide a clear estimation of the interface persistence lengthscale. We also show how the peaks and antipeaks analysis that our group has developed to better understand polar-apolar and positive-negative alternations in the bulk structure factor $S(q)$ can be recast to provide novel and insightful information about interfacial reflectivity. The analysis dissects the nearly featureless overall normalized reflectivity into a rich collection of peaks and antipeaks that provides significant insight into the location and width of apolar and charged layers. The peaks and antipeaks analysis captures fine structural details within layers –including the pattern of charge alternation that is non-lateral– associated with the preferential arrangement of charged species within a polar layer.

1 Introduction

In the past few years, a prominent trend in ionic liquids (ILs) research has been to mix them or combine them with conventional solvents to improve viscosity or gain access to other advantageous features in the bulk state.[1–6] Our computational study focuses instead on accessing modified properties at the vacuum boundary. In particular, we explore the segregation at the interface based on polarity of the subcomponents in the mixture of 1-Methyl-3-octylimidazolium Octylsulfate (C[8]-mim$^+$/C[8]-OSO$_3^-$) with 1-Ethyl-3-methylimidazolium Ethylsulfate (C[2]-mim$^+$/C[2]-OSO$_3^-$) and the dissipation of local structure away from the interface.

We explore two regimes, one in which a film is thin and there simply isn't any bulk-like liquid at its center; in this case the film is highly organized based on charged and apolar sublayers. We also study the case in which the film is thicker and a distinct bulk-like region can be detected away from the interface. In light of many intriguing questions regarding structural memory effects away from IL interfaces,[7–13] we investigate in detail its persistence lengthscale.

From a technical computational perspective, we use this article to bring to light important issues regarding IL simulation convergence and in particular *the difference between a well-equilibrated simulation and a well averaged density profile* away from the interface. There is a significant body of work on ILs at interfaces, but we believe that in many cases thorough structural convergence of atomic density profiles away from the interface may have not been properly achieved. For reasons that will become clear, getting this right for simulations of ILs at interfaces is much harder than properly converging the pair distribution function for the bulk. Getting these density profiles correctly converged is crucial since ***both*** the bulk liquid and interfacial film configurations are intrinsically structurally heterogeneous. The objective is to *unequivocally distinguish the density oscillations away from the interface that are solely due to the break in symmetry from the very similar oscillations naturally occurring in the bulk* due to polar-apolar structural heterogeneity that gives rise to the prepeak or first sharp diffraction peak in its structure function $S(q)$. This is important for example to properly compute and analyze the system's X-ray or neutron reflectivity.

Since both the bulk and adjacent interface have apolar and polar regions, the main difference in the structural heterogeneity between the two is orientational. To properly compute the interfacial density profiles, it is not enough to have a properly converged simulation. We must also ensure that sufficient orientational averaging of the structural heterogeneities in the bulk-like region away from the interface is achieved. A rule of thumb is that the time scale for this should be consistent with or longer than that for the decay of the lowest q-peak in $S(q,t)$ of the bulk. Otherwise, density profiles away from the interface will inevitably

display the "instantaneous" oscillatory behavior of the structurally heterogeneous bulk.

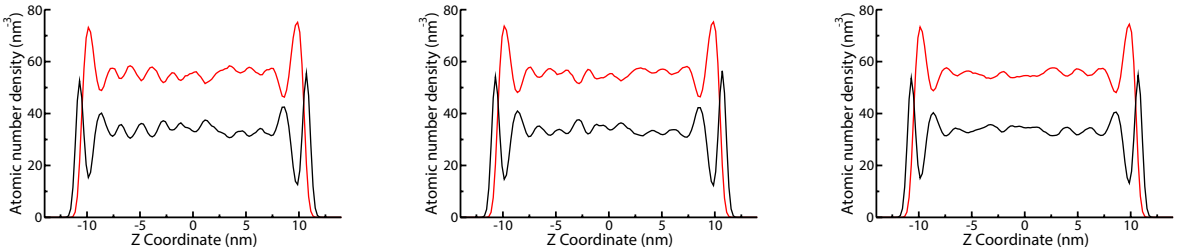

(a) first-5ns (b) first-10ns (c) first-20ns

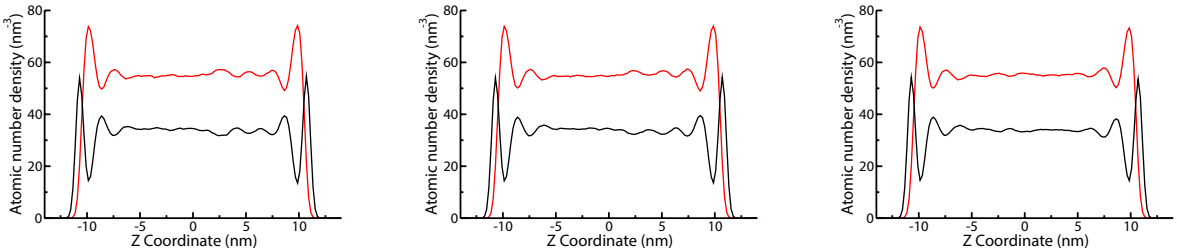

(d) first-40ns (e) first-60ns (f) first-180ns

Figure 1: For a 50% mixture of C[8]-mim$^+$/C[8]-OSO$_3^-$ and C[2]-mim$^+$/C[2]-OSO$_3^-$ at 425K, atomic number density for apolar (black) and polar (red) subcomponents averaged over cumulatively longer times. Atoms belonging to the polar and apolar subcomponents are defined in the methods section and highlighted in the right panel of Fig. 3.

Fig. 1 shows an example of this. In all cases, the interfacial structure and the adjacent bulk structure are likely properly converged. However, the density profiles are not. Only after averaging over a large number of properly converged bulk liquid configurations on a time scale of 200 ns the density profile at the center of the film becomes flat and the persistent oscillations in the profile solely due to the break in symmetry at the interface. The reader must understand that it is not that at 180 ns the system was finally properly equilibrated; an average of the density profiles over the last 10 ns of simulations will likely be as oscillatory as one for the first 10 ns. Instead, the last profile in Fig. 1 appears converged because we have averaged over the many random proper equilibrium orientations of domains associated with the slowest structural heterogeneities in the bulk vicinal to the interface. In Fig. S1

of the SI we provide a plot of the time-dependent mean squared deviation between density profiles with respect to the fully averaged one; for these ILs at 425 K, the averaging time to capture density fluctuations that are only due to the interface should be on the order of 0.1 μs.

With well converged density profiles away from the interface, we focus on the calculation and analysis of the system's normalized X-ray reflectivity. Reflectivity studies provide exquisitely detailed information about layering of species at the interface.[14–29] Under the approximations used here, the atomic density profiles away from the interface are convoluted with atomic X-ray form factors to generate via Fourier transformation the normalized reflectivity. We highlight that the normalized reflectivity at the vacuum interface is not a simple sum of the reflectivities associated with the atomic electron densities; cross-terms generate interferences.[17] Akin to our prior work in the bulk,[30–35] and perhaps different from other studies, we propose to partition the normalized reflectivity into carefully selected terms associated with subcomponents of the liquid; this helps reveal information about apolar and charge alternations away from the interface.

2 Computational Methods

All molecular dynamic simulations were conducted using the GROMACS package[36,37] and we used the Canongia-Lopes and Padua[38,39] and Optimized Potentials for Liquid Simulations All-Atoms (OPLS-AA) force fields[40–42] except that all charges were scaled by a factor of 78% in order to properly capture the experimentally known viscosity of C[2]-mim$^+$/C[2]-OSO$_3^-$($\approx$15 cP[43] at 353.15K) while still reproducing its experimental structure function $S(q)$.[44] To the best of our knowledge, experimental structural and viscosity data for C[8]-mim$^+$/C[8]-OSO$_3^-$ were unavailable for comparison.

Fig. 2 shows a plot of S(q) in the bulk for mixtures of the two liquids at different concentration ratios. From it we see that C[8]-mim$^+$/C[8]-OSO$_3^-$ has a first sharp diffraction peak

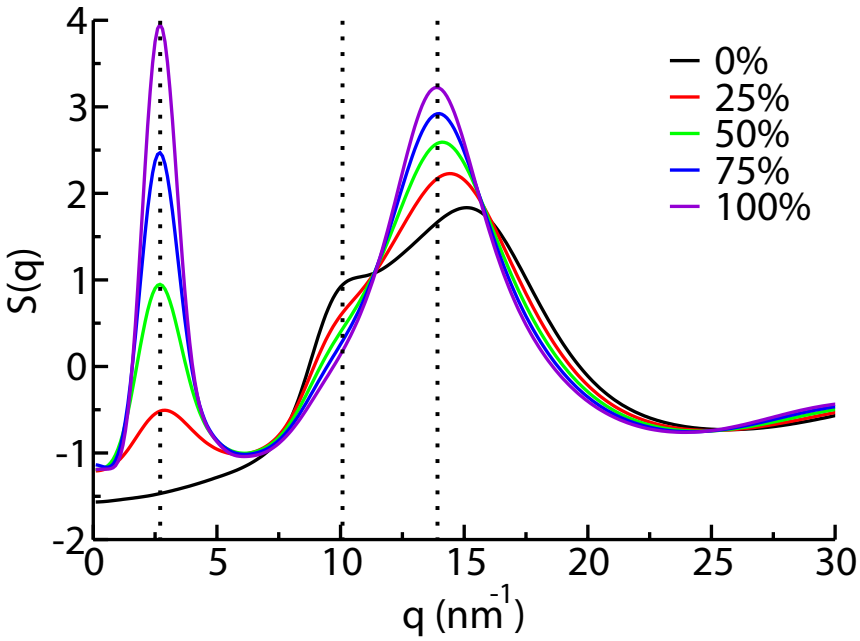

Figure 2: Structure function of IL mixture (C[8]-mim$^+$/C[8]-OSO$_3^-$-C[2]-mim$^+$/C[2]-OSO$_3^-$) as a function of the relative percentage of C[8]-mim$^+$/C[8]-OSO$_3^-$.

below 5 nm^{-1} characteristic of polar-apolar structural heterogeneity; this peak is absent in the case of C[2]-mim$^+$/C[2]-OSO$_3^-$. Both liquids show typical charge alternation regions at about 10 nm^{-1} and the common adjacency peak between 13 and 20 nm^{-1}. Mixtures at different concentration ratios have first sharp diffraction peaks of different intensities. For our study of the vacuum interface we focus on the 50% molar ratio case that in the bulk clearly preserves a significant amount of domain structural heterogeneity.

We are interested in describing two scenarios, one in which both the interface and a bulk-like region are present and another in which the film is thin and our system is purely dominated by the structured interface. For the first case our simulation contains 1500 ion pairs of each type (6000 ions) while for the second 150 pairs of each type (600 ions). Our explicit choice of a scaled-charges force-field or in general a fixed-charges force-field at an interface has obvious limitations since the dielectric constant changes significantly across the boundary. A polarizable force field should more appropriately accommodate these changes;

however, simulations with thousands of polarizable ions for hundreds of nanoseconds are still prohibitively expensive switching the aforementioned limitation for another associated with the collection of sufficient statistics to converge the density profile. For this study, we find that addressing the second limitation is significantly more important. With more resources in the future, studies with polarizable force fields should be carried out in comparison. In our study, capillary waves are those arising from simulation; no attempt has been made to modify our computed density profiles to account for lower wavelength smearing.

2.1 Simulation Protocols

To prepare our systems for slab simulations, we initially performed an energy minimization in the bulk using the steepest descent algorithm. Each system was then equilibrated at 300 K by slowly increasing charges from 1% to their target value while decreasing pressure from 50 bar to 1 bar in 4.2 ns. During this preliminary equilibration step, the V-rescale thermostat[45] and Berendsen barostat[46] as coded in GROMACS[36,37] were used. Following this, a simulated annealing protocol was used in which the temperature was increased to 750 K and slowly decreased to 650 K in 8 ns. Further equilibration in the bulk at constant temperature and pressure was carried out using the Nose-Hoover thermostat[47,48] and the Parrinello-Rahman barostat[49] at 650 K for 60 ns. Final box dimensions in the bulk for the largest simulation box with 3000 ion pairs were 8.66023 nm $\times$ 8.66023 nm $\times$ 25.98068 nm. During equilibration, the Leap-frog algorithm[50] was used with a time step of 1 fs to integrate equations of motion. The Particle Mesh Ewald (PME)[51,52] method with B-spline interpolation of order 4 and Fourier grid spacing of 1.2 Å was used to compute electrostatic interactions. Short range Coulomb and Lennard-Jones cutoffs were set to 1.5 nm.

For our simulations in the slab configuration, we used the EW3DC[53,54] PME protocol that includes the Yeh-Berkowitz correction approximating the 2-D Ewald Sum. The already well-equilibrated bulk system was further equilibrated in the NVT ensemble for 5 ns. After that, the system was placed at the center of a 8.66023 nm $\times$ 8.66023 nm $\times$ 103.92272

nm box so that the length of the empty space between periodic slabs (77.94204 nm) was significantly larger than the lateral box length. According to the original studies by Yeh and coworkers,[53,54] this ensures the applicability of the EW3DC algorithm. Now in the presence of the interface, these simulations were then followed by a 5ns NVT equilibration and a 8 ns simulated annealing in which the temperature was increased to 750 K and slowly decreased to our final target temperature of 425 K. Production runs in the slab configuration at 425 K were 200 ns in duration and the last 180 ns were used for analysis. For slab simulations, a time step of 1 fs and the leap-frog integrator were used to integrate equations of motions.

Separately, for the calculation of bulk structure functions in Fig. 2, a protocol similar to that used here for equilibrating the bulk structure was used, except that the final target temperature was 425 K to match that of the interfacial studies and production runs were 60 ns in duration. For all systems, reported results in this article are from production runs at 425K.

2.2 The Partitioning of the Normalized Reflectivity in Terms of Ionic-Liquid Structural Subcomponents

Since from our classical molecular dynamics simulations what we get is atomic positions, we aim to compute the reflectivity in terms of those. The q-dependent X-ray reflectivity is defined as[55–57]

$$R(q) = \left(\frac{4\pi r_e}{qA_{uc}}\right)^2 |F(q)|^2 \tag{1}$$

where r_e, A_{uc} are the electron radius and unit area respectively and

$$F(\mathbf{q}) = \sum_j f_j(q) e^{i\mathbf{q}\cdot\mathbf{r_j}}.$$

In our case A_{uc} is the simulation box area in the X-Y plane. In $F(\mathbf{q})$, the sum extends over all atoms j with q dependent X-ray atomic form factor $f_j(q)$ and is evaluated for $\mathbf{q} = (0, 0, q)$

corresponding to the reflectivity condition. To preserve the desirable concept of a thermally broadened density profile that gives rise to a reflectivity intensity, we cast this sum in terms of integrals of time averaged atomic densities $\rho_i(z)$

$$\sum_i \int_{-\infty}^{\infty} \rho_i(z) f_i(q) e^{iqz} dz = \sum_i f_i(q)\rho_i(q) = \sum_i F_i(q) = F(q),$$

where i now labels atom-types. This commonly used approximation[22,55–64] where the ensemble average is taken for the density instead of for the norm squared of $F(q)$ implies that thermal roughness is included but there is no roughness correlation at the interface. In practice, this means that such height-height correlations are very short-ranged.[62] Therefore, Eq. 1 becomes

$$R(q) = \left(\frac{4\pi r_e}{qA_{uc}}\right)^2 \left| \sum_i \int_{-\infty}^{\infty} f_i(q)\rho_i(z) e^{iqz} dz \right|^2.$$

Numerically, it is advantageous to take Fourier transforms of the derivatives of the atomic number densities because these become zero both in the positive and negative directions away from the interface. This is achieved via integration by parts.[61,65]

$$\begin{aligned} R(q) = \left(\frac{4\pi r_e}{qA_{uc}}\right)^2 \left| \sum_i \int_{-\infty}^{\infty} \frac{f_i(q)\rho_i'(z) e^{iqz} dz}{iq} \right|^2 &= \left(\frac{4\pi r_e}{q^2 A_{uc}}\right)^2 \left| \sum_i \int_{-\infty}^{\infty} f_i(q)\rho_i'(z) e^{iqz} dz \right|^2 \\ = \frac{R_F(q)}{\rho^2 A_{uc}^2} \left| \sum_i \int_{-\infty}^{\infty} f_i(q)\rho_i'(z) e^{iqz} dz \right|^2 &= R_F(q) \left| \frac{1}{\rho_\infty} \sum_i \int_{-\infty}^{\infty} f_i(q)\rho_i'(z) e^{iqz} dz \right|^2, \end{aligned}$$

so that the normalized reflectivity becomes

$$\frac{R(q)}{R_F(q)} = \left| \frac{1}{\rho_\infty} \sum_i f_i(q) \int_{-\infty}^{\infty} \rho_i'(z) e^{iqz} dz \right|^2. \tag{2}$$

Where ρ is the bulk liquid electron density away from the interface and $\rho A_{uc} = \rho_\infty$; $R_F(q)$ corresponds to the reflectivity of a featureless step function interface.

To better understand the contribution of different liquid subcomponents to the normalized reflectivity, we partition $\frac{R(q)}{R_F(q)}$ into contribution of polar and apolar subcomponents as

well as further subdivide the polar part into positive and negative sub-ionic contributions. For simplicity, all atoms in C[2]-mim$^+$ are considered part of the positive partition and all atoms in C[2]-OSO_3^- are considered part of the negative partition. The equivalent atoms in C[8]-mim$^+$ (C[8]-OSO_3^-) are considered positively (negatively) charged whereas the rest are considered part of the apolar partition. With this definition we have

$$\frac{R(q)}{R_F(q)} = \left| \frac{1}{\rho_\infty} \left\{ \sum_{k\in(+)} f_k(q) FT(\rho'_k(z)) + \sum_{l\in(-)} f_l(q) FT(\rho'_l(z)) + \sum_{m\in(apolar)} f_m(q) FT(\rho'_m(z)) \right\} \right|^2, \tag{3}$$

where the k, l, m indexes span the atoms included in each subclass. Each of the individual sums is a complex function of q and the norm squared in Eq. 3 results in six different real terms.

$$\frac{R(q)}{R_F(q)} = \frac{R_+(q) + R_-(q) + R_{apolar}(q) + R_{+/-}(q) + R_{+/apolar}(q) + R_{-/apolar}(q)}{R_F(q)}. \tag{4}$$

The analogous splitting based only on polar and apolar subcomponents is

$$\frac{R(q)}{R_F(q)} = \frac{R_{polar}(q) + R_{apolar}(q) + R_{polar/apolar}(q)}{R_F(q)}. \tag{5}$$

The reader can find the general derivation for an arbitrary number of disjoint partitions in the Supporting Information (Eqns. S1 through S6). The equations in this section should be contrasted with the polar-apolar and positive-negative partitions of the bulk structure function S(q) as derived in our prior publications.[31–35,66–68] Just like in the analysis of the bulk structure function $S(q)$,[30–35,66,68] the self and cross terms in Eqns. 4 and 5 can give rise to peaks and antipeaks with rich underlying information about IL structure but in this case under a situation of broken symmetry. Just like with the bulk S(q), this information is concealed in $\frac{R(q)}{R_F(q)}$ due to massive cancellations of out-of-phase density oscillations.

In this article, we only study the normalized reflectivity of our largest system for which interfacial structural oscillations completely decay and a bulk-like liquid is observed beyond

it. The approximation is that there is only one interface, and away from it the bulk liquid extends to infinity. Due to the use of the kinematical approximation[61] and limitations associated with our box length, $R(q)/R_F(q)$ should only be considered accurate above ≈ 0.5 nm^{-1}.

3 Results and Discussion

3.1 Real Space Analysis of the Density Profiles

We study two systems, one in which our 50% mixture of two ILs results in a film that is about 6 nm in thickness and a second where the thickness is about 24 nm. Figures 3 (left) and (right) show color-coded density profiles highlighting polar and apolar subcomponents with the polar subcomponent further divided into the contribution of larger and smaller ions. Associated with these profiles we also show composite snapshots of our systems consisting of 90 frames each spaning from 20 ns to 200 ns in the production run.

We find that the 6 nm film is highly ordered. Since the persistence lengthscale of each interface is longer than 3 nm, density oscillations from each side do not completely decay but instead meet in the middle and are correlated. This film is essentially two correlated interfaces with no bulk liquid in between. Instead, we find for our 24 nm film that after about two oscillation cycles of the subcomponent density profiles these go mostly flat indicating a complete decay lengthscale of about 6 nm. Interestingly, both for the narrow and wider films, trends are quite similar with an outermost layer being apolar followed by charged contributions of the larger ions and then from the smaller ions followed by a second apolar layer.

Figures 4 (left) and (right) reveal that the polar layer is actually two different adjacent layers that partially overlap. Approaching the system from the vacuum interface one finds first the charged heads of C[8]-mim^+/C[8]-OSO_3^- and deeper the charges of C[2]-mim^+/C[2]-OSO_3^-. Overall, this results in a first polar slab that is significantly thicker than the adjacent

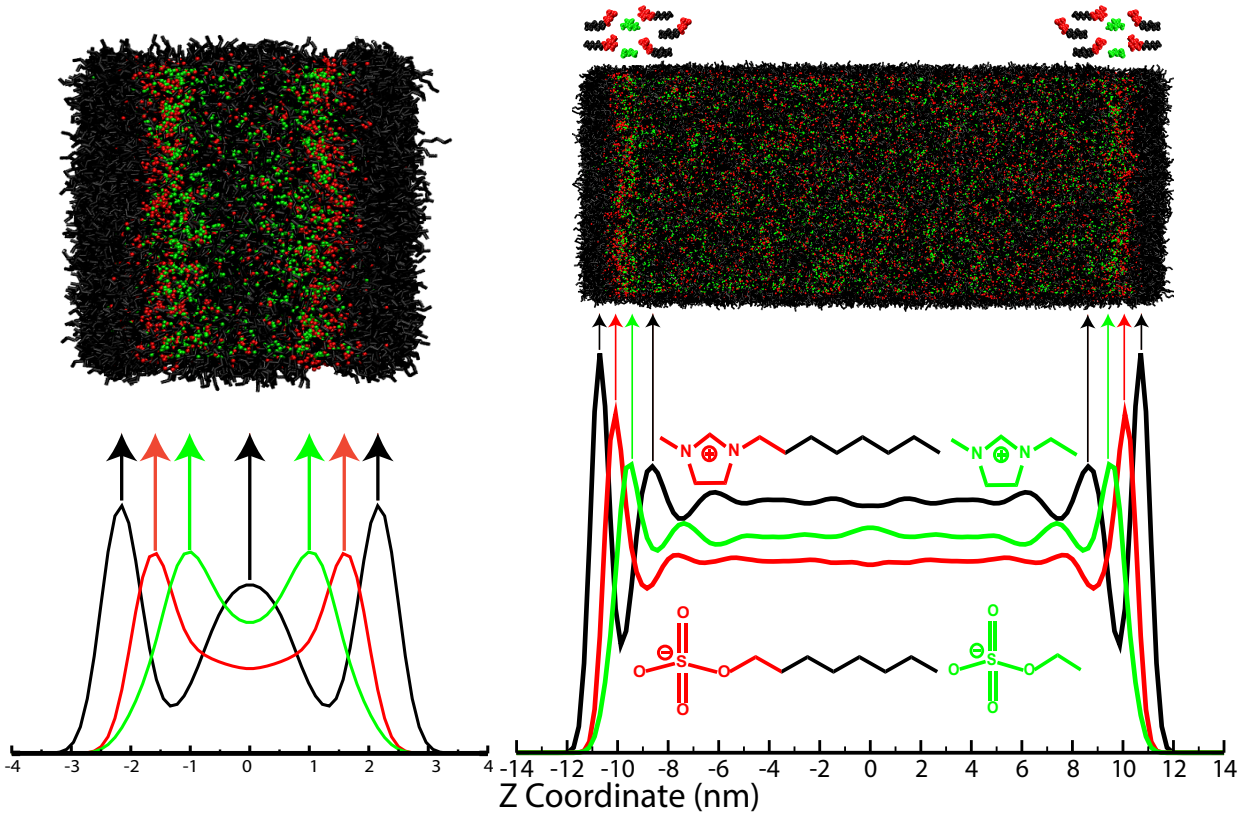

Figure 3: For our two systems, graphs show atomic density profiles. The profile for apolar tails is in black, for the polar subcomponents consisting of the cationic and anionic heads of C[8]-mim$^+$/C[8]-OSO$_3^-$ is in red and for the C[2]-mim$^+$/C[2]-OSO$_3^-$ ions is in green. Atomic components included in each profile are also depicted as sticks and color-coded on the right side. On top of each set of density profiles, we show an overlay of 90 frames across the full production trajectory highlighting the position along the Z-direction where individual density maxima occur. For our largest system, atop of the simulation frames we also show a cartoon representation of the unsymmetric distribution of longer- and shorter-tail ions away from the interface. This pattern of charge alternation across ions of different size that is not lateral (i.e. not in the X-Y plane) has an effect on the normalized reflectivity which can be teased out by the peaks and antipeaks analysis.

outer apolar layer.

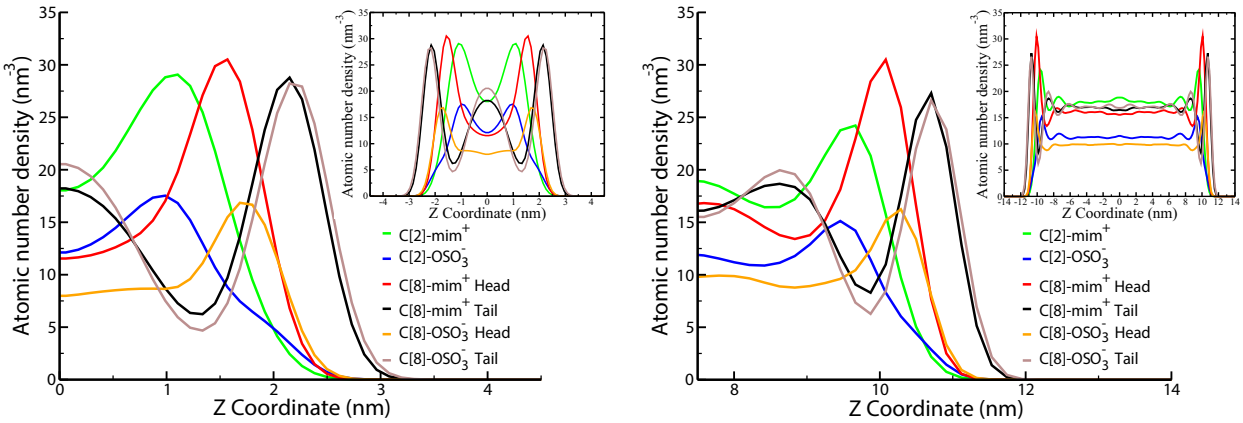

Figure 4: Color-coded symmetrized (about the center of the box) density profiles in the vicinity of the interface for positive, negative and apolar sub-ionic components for the small (left) and large (right) films. In all cases, insets show corresponding symmetrized full density profiles. For the larger film, and as a function of distance from the vacuum interface we find first an apolar monolayer, followed by the charges of the larger ions and then by those of the smaller ions. A second apolar bilayer forms beyond this as highlighted in Fig. 5 as well as in a cartoon format atop Fig. 3 (right).

A more nuanced analysis of the interface results from the analysis of the orientational order parameter $P_1(\theta)$ in Fig. 5 equivalent to the signed Z-component of a unit vector connecting the position of fourth-to-last and last (terminal) carbon atoms in the tail of C[8]-mim$^+$(almost equivalent results are obtained from the orientational analysis of C[8]-OSO$_3^-$; data not shown). As expected, we notice that tails at the interface point towards the vacuum. Connected to these tails are charged subcomponents of C[8]-mim$^+$ and C[8]-OSO$_3^-$, and adjacent to these but deeper in the liquid-phase are C[2]-mim$^+$ and C[2]-OSO$_3^-$ ions. However, in order to form a second apolar layer away from the interface, a fraction of the tails of the long ions still within the first charged density peak must point inside towards the liquid. In other words, longer ions in the first density oscillation must contribute to the outer apolar layer but also to the inner apolar bilayer.

Vertical and horizontal dashed blue lines in Fig. 5 highlight the location for orientation change of C[8]-mim$^+$ ions. To the left of the first vertical dashed line $P_1(\theta)$ is negative,

corresponding on average to tails pointing towards the vacuum interface. In between vertical lines $P_1(\theta)$ is positive, meaning that here on average apolar tails are pointing inwards towards the liquid phase. These inward pointing tails contribute to the outermost portion of the second apolar density peak (the apolar density profile is shown in the red in Fig. 5). Past the second dashed vertical line, $P_1(\theta)$ is again negative indicating that on average the innermost portion of the second density peak has tails pointing outward toward the vacuum interface forming what we interpret as a bilayer. In other words, the first apolar density peak is oriented towards the vacuum, whereas the second apolar density peak is first oriented towards the inside liquid phase but deeper it is oriented towards the vacuum interface. This is highlighted by the color-coded ion models atop Fig. 5. Beyond these oscillations in $P_1(\theta)$ we see the function decay to zero showing no preferential tail orientations consistent with bulk-like behavior. For simplcity, we do not include the role of the smaller ions in this figure, but it should be understood that a significant accumulation of these occur just after the first layer of charge from the larger ions.

Whereas most of the charge alternation –the hallmark feature of ionic liquids– occurs laterally (not along Z), and is therefore not detectable by specular reflectivity, there is a Z-dependent component due to the distinctly different preference for the longer ions at the vacuum interface. Such intra-layer behavior should be almost impossible to pick out from $\frac{R(q)}{R_F(q)}$, but becomes clear using the peaks and antipeaks analysis from section 3.2.

Whereas Fig. 3 shows an outer layer that is completely covered in apolar tails, this is only because these are composite snapshots. Individual snapshots show enhancement of tails at the interface but not full coverage (see comparison between instantaneous and composite snapshots in Fig. 6). Similar behavior has been observed for a different system in reference 69. In our study, this is in part due to the fact that charged ions have to contribute both to the outer apolar monolayer and the inner apolar bilayer.

From the integration of our density profiles, we can provide estimates to the commonly reported[27,70] surface area per hydrophobic tail at the vacuum interface. The estimation

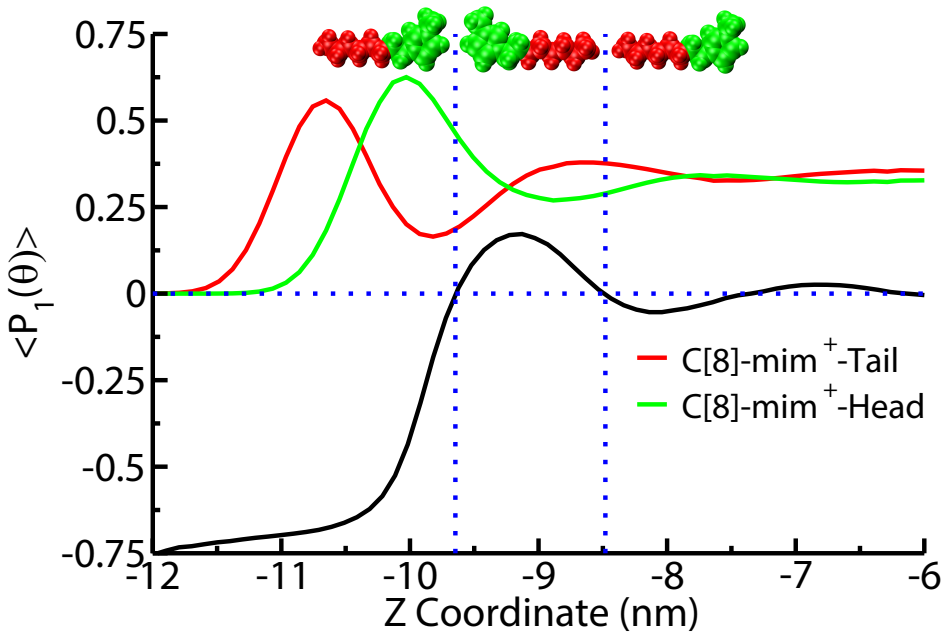

Figure 5: For our thicker film, in black, order parameter $P_1(\theta)$ denoting the Z-component of a unit vector pointing from fourth-to-last carbon to the terminal carbon in the tail of C[8]-mim$^+$. Negative values of this function correspond to outward (towards the vacuum interface) pointing tails whereas positive values correspond to inward (towards the bulk) pointing tails. Overlayed and not up-to-scale in red and green are charged and apolar density profiles for the same cation respectively. Molecular representations show schematically the direction of ions associated with the order parameter.

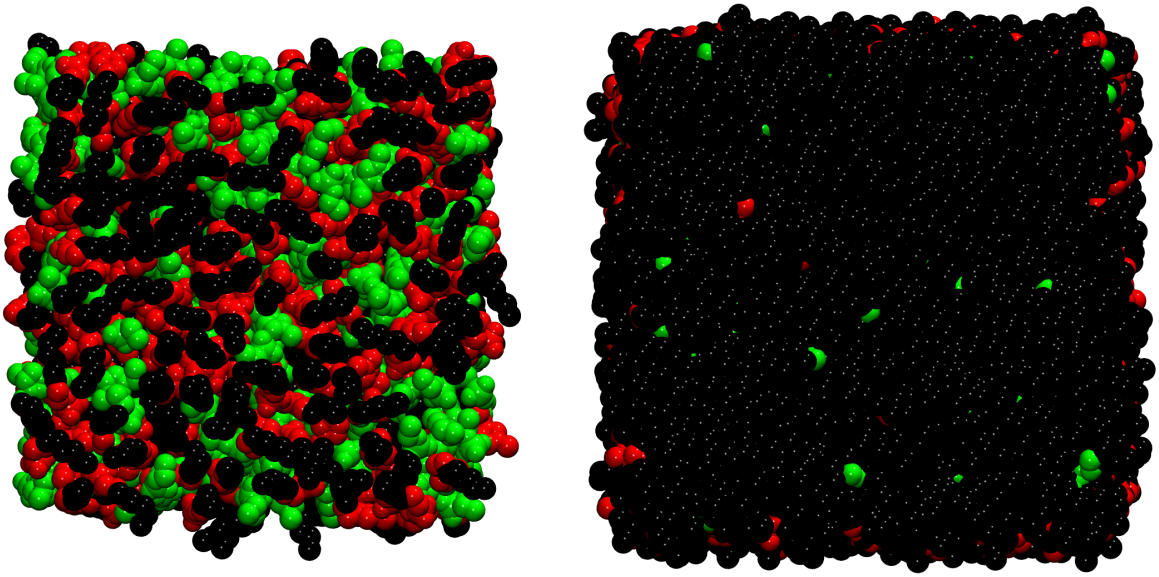

Figure 6: For the thinner film at the vacuum interface, top view (Z-axis coming out of the page) of (left) a single simulation snapshot highlighting apolar tails (black), polar cationic and anionic heads of C[8]-mim$^+$/C[8]-OSO$_3^-$ (red), and C[2]-mim$^+$/C[2]-OSO$_3^-$ (green); (right) ninety simulation frames overlapped according to the same representation scheme spanning the last 180 ns of the production run. Similar results are obtained for the thicker film (data not shown).

depends on the value one chooses as inner limit to this integral. If we chose to integrate up to the Z value corresponding to $P_1(\theta) = 0$, the area per tail is 0.32 nm^2, if instead we integrate up to the first minimum (first maximum) of the apolar density profile, the value is 0.37 nm^2 (0.80 nm^2).

3.2 Prediction and Analysis of the Normalized Reflectivity

For Ionic Liquids in the bulk with significant apolar tails, two types of alternations exist giving rise to prominent peaks and antipeaks in subcomponents of $S(q)$.[30–34] At low q values (commonly below 5 nm^{-1}) there is a prepeak that is due to the alternation between charges and tails –same class correlations (polar-polar, apolar-apolar) of atomic subcomponents give rise to peaks whereas opposite class (polar-apolar) correlations result in what we have called in prior publications antipeaks–; for our composite system in the bulk phase this is depicted in Fig. 7 (left). Instead, at $q \approx 10$ nm^{-1}, one finds the hallmark characteristic of all ILs which is positive and negative charge alternation –same class correlations (positive-positive, negative-negative) between ionic subcomponents give rise to peaks whereas opposite class correlations (positive-negative) result in antipeaks–; this can be clearly seen from Fig. 7 (right).

Fig. 8 (left) shows the computed normalized reflectivity $\frac{R(q)}{R_F(q)}$ for our IL mixture as well as its polar-polar, apolar-apolar and polar-apolar subcomponents based on Eqn. 5. As far as we are aware, no experimental reflectivity data exist for our mixture of ILs, however, the reader is encouraged to compare our computational results against the reflectivity of other ILs showing similar characteristics (see for example Fig. 6 in reference 22, top curves in Fig. 5 (a) and (b) of reference 65 and in particular the reflectivity of $C_n$mim/Ntf_2 for n in the range 6-8 in Fig. 1 of reference 27).

Except for a very small dip only noticeable when plotted in log-scale at about 6.6 nm^{-1} –which we discuss below in section 3.2.2– the overall $\frac{R(q)}{R_F(q)}$ in Fig. 8 (left) appears to be a featureless sigmoidal-like function. Instead, the polarity splitting of $\frac{R(q)}{R_F(q)}$ reveals the

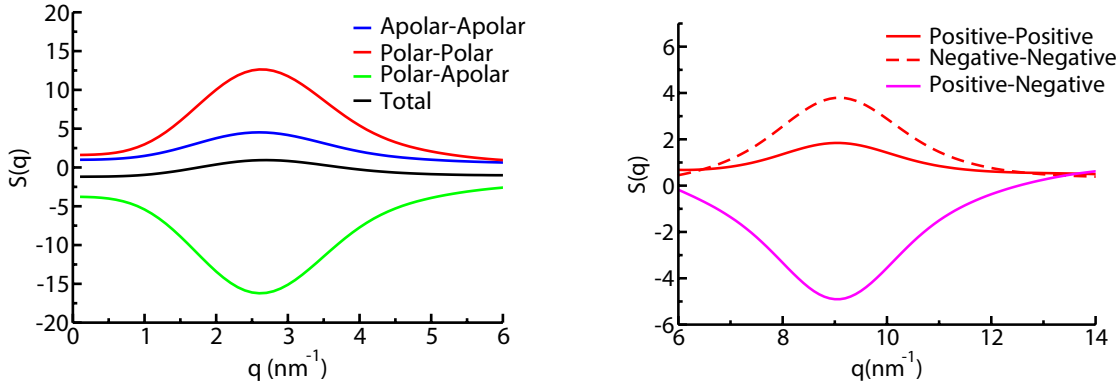

Figure 7: (Left) Polarity partition of S(q) in the region corresponding to the prepeak. (Right) Positive-negative partition of S(q) in the region corresponding to charge alternation.

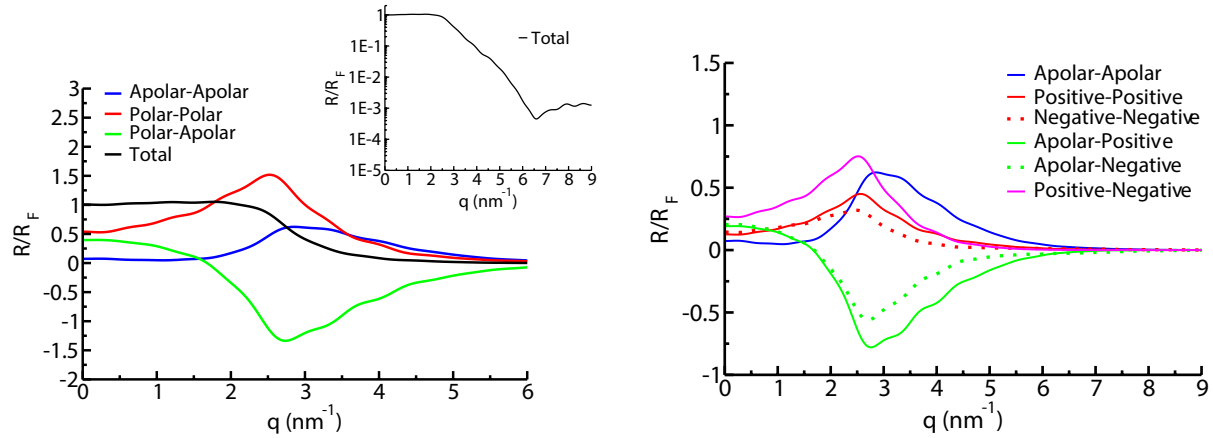

Figure 8: (Left) Normalized reflectivity $\frac{R(q)}{R_F(q)}$ and corresponding apolar-apolar, polar-polar and polar-apolar subcomponents as defined in the methods section. Inset shows $\frac{R(q)}{R_F(q)}$ in logarithmic scale. (Right) $\frac{R(q)}{R_F(q)}$ and its apolar-apolar, positive-positive, negative-negative, apolar-positive, apolar-negative and positive-negative subcomponents.

underlying structure of the interface. Two peaks corresponding to polar-polar and apolar-apolar correlations can be observed with a corresponding antipeak for the polar-apolar cross-term. The sum of these three curves each with a clearly identifiable maximum or minimum gives rise to the overall peakless $\frac{R(q)}{R_F(q)}$.

Fig. 8 (left) should be contrasted against Fig. 7 (left) because there is a clear connection between the peaks and antipeaks observed for subcomponents of $\frac{R(q)}{R_F(q)}$ and those associated with the first sharp diffraction peak or prepeak in $S(q)$ of the bulk mixture. The interface-patterned density oscillations of polar and apolar liquid subcomponents exist also in the bulk but with random time-dependent orientations; this is why Fig. 8 (left) and Fig. 7 (left) are qualitatively so similar. From Fig. 8 (right) we see that consistent with the behavior at q values associated with the first sharp diffraction peak in the bulk, correlations between positively and negatively charged ionic components contribute to $\frac{R(q)}{R_F(q)}$ as peaks;[31,33,34] this is because in this q-region these are same-type –both polar– correlations. This is in contrast to the typical antipeak observed for positive-negative subcomponents of $S(q)$ in the charge alternation region around 10 nm^{-1} where they behave as opposite-type –opposite charge– correlations (see Fig. 7 (right)). Splittings of $\frac{R(q)}{R_F(q)}$ in Fig. 8 (right) based on Eq. 4, highlight same-type positive-positive and negative-negative behavior (peaks) as well as positive-apolar and negative-apolar antipeaks at similar but not identical q values. This is the same polar-apolar layering highlighted in Fig. 8 (left) which can also be gleaned in real space from Fig. 3 (right).

3.2.1 What in Practice Determines the Peak Position of the Subcomponents of $\frac{R(q)}{R_F(q)}$?

We notice that the peak position for polar-polar correlations in Fig. 8 (left) and those for positive-positive, negative-negative and positive-negative correlations in Fig. 8 (right) appear at lower q values than that for the apolar-apolar correlations. What makes this so?

Figures 9 show symmetrized (about the middle of the simulation box) real-space density

profiles for polar and apolar subcomponents in the left panel and apolar, positive and negative subcomponents in the right panel. We see from Fig. 9 (left) that the first density peak for the apolar subcomponent is narrow (see also column 5 in Tab. 1). This means that the first apolar layer is compact and organized. Instead, the first polar layer is formed by overlapping charge layers first from C[8]-mim$^+$/C[8]-OSO$_3^-$ and second from C[2]-mim$^+$/C[2]-OSO$_3^-$. It is this difference in first layer thickness as well as the distance in real space between peaks that results in the charged subcomponent contributing at lower q values. We see from Tab. 1, that the q value associated with the maximum in subcomponents of $\frac{R(q)}{R_F(q)}$ correlates reasonably well both with the spacing between the first two real-space density maxima as well as the width of each first layer.

Table 1

Subcomponent	q (nm^{-1})	$2\pi/q$ (nm)	Peak distance (nm)	First peak width (nm)
Polar	2.52	2.49	2.36	2.84
Apolar	2.85	2.20	2.06	2.08

Based on Fig. 8, column 2 shows the q value for maximum. Using this q value, column 3 shows the real space distance $2\pi/q$; column 4 shows the distance between first and second density maxima in Fig. 9 (left), and column 5 the approximate width (bottom-to bottom) of the first density maximum in Fig. 9 (left).

The polar and apolar density subcomponents depicted in Fig. 9 (left) can be fitted to an analytical function of the form (see Fig. S2 in the SI),

$$\rho_i = \{1 + erf(\frac{z - z^{'}}{\sigma})\}\{A \cdot sin[k(z - z_0)] \cdot e^{-\frac{z-z_0}{l_0}} + \frac{\rho_{i,\infty}}{2}\} \tag{6}$$

where l_0 controls the persistence length of oscillations into the bulk-like liquid phase, k, A the periodicity and amplitude, σ in the error function controls the sharpness of the interface and z_0, $z^{'}$ are fitting parameters controlling the location of the interface. It is clear from this expression that even though a single sine function is involved, the density oscillations will not be governed by a unique periodicity; furthermore, peaks will not be symmetric. In practice, the first density peak's width is most heavily influenced by the error function

controlling the sharpness of the interface, while the second density oscillation is asymmetric due to the exponential controlling the spatial decay of oscillations.

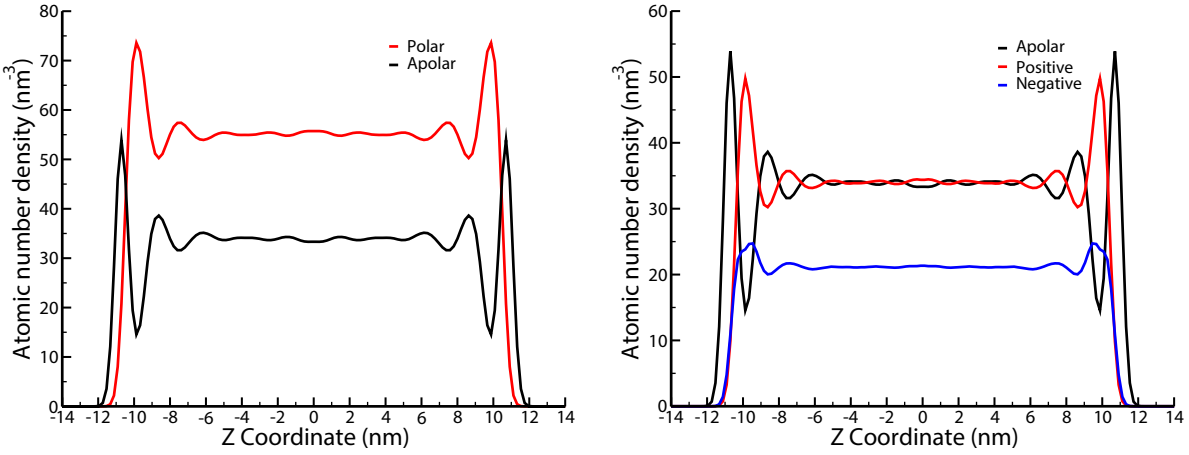

Figure 9: For our larger film system, we show color-coded symmetrized (about the center of the box) density profiles for polar and apolar subcomponents (left) and apolar, positive and negative subcomponents (right).

3.2.2 Structural Effects of Mixing: Charge and Polarity Alternation Along the Z-direction at the Interface

For ILs, one expects that at the liquid-vacuum interface charge alternation should have a majority component that is lateral and cannot be detected from specular reflectivity which only probes density profiles along the Z-direction. However, in our system the larger C[8]-mim$^+$/C[8]-OSO$_3^-$ ions have a preference for the interface when compared with those in C[2]-mim$^+$/C[2]-OSO$_3^-$. In other words, our system is likely significantly more polar beneath the apolar blocking layer than would otherwise be expected in the case of neat C[8]-mim$^+$/C[8]-OSO$_3^-$. This concentration gradient (large ion charges close to the surface and small ion charges deeper in) results in an additional form of charge-charge alternation that occurs along the Z direction as opposed to in the X-Y plane. It is not unreasonable to expect such Z-dependent broken symmetries in charge alternation to occur even in the case of neat ILs when cations and anions possess different size, geometry or hydrophobic char-

acteristics; however, capturing this from the experimental $\frac{R(q)}{R_F(q)}$ should be quite challenging and this is where the peaks and antipeaks analysis becomes most useful.

From Fig. 8 (left) we see that the black line provides scant information on the q value for polar-apolar alternation patterned by the interface and even less on phenomena occurring at shorter distances (larger q). Yet, hint of a structural feature can be gleaned in logarithmic scale at around 6.6 nm^{-1}. We will show that this feature, which is of very low intensity, is related to cancellations of self and cross terms in $\frac{R(q)}{R_F(q)}$ associated with the real-space out-of-phase oscillation of the density profiles of large and small ions.

To address the complexity of extracting higher q (lower distance) information from $\frac{R(q)}{R_F(q)}$ we further split polar contributions to $\frac{R(q)}{R_F(q)}$ into those of C[8]-mim^+/C[8]-OSO_3^- as separate from those of C[2]-mim^+/C[2]-OSO_3^-. By doing this we are able to identify in reciprocal space (1) the q values at which real-space charge oscillations across large and small ions species constructively or destructively interfere and (2) how the Z-dependent distributions of large and small ion charges differently interfere with the apolar layers.

Figure 10 shows self and cross correlations contributing to $\frac{R(q)}{R_F(q)}$. All self terms are positive-definite and peak approximately at the position corresponding to the bulk prepeak; this is simply indicative of polar-apolar alternations away from the interface. More interesting are the cross terms linking the charged subcomponents of C[8]-mim^+/C[8]-OSO_3^- and C[2]-mim^+/C[2]-OSO_3^- as well as each of these with the apolar subcomponent. In Fig. 10, the dashed green line coupling charges in C[8]-mim^+/C[8]-OSO_3^- with those in C[2]-mim^+/C[2]-OSO_3^- grows to reach a positive peak at low q followed by a negative antipeak at higher q value. Instead, brown and purple dashed lines coupling charges with apolar subcomponents decrease to form a negative antipeak and then approach zero at higher q values. The purple curve goes through a second maximum before decaying to zero. We can explain this very generic reciprocal space cross-term behavior by using a highly simplified model in which C[8]-mim^+/C[8]-OSO_3^- and C[2]-mim^+/C[2]-OSO_3^- charges as well as the apolar subcomponent have identical real space density profiles but distinct spatial shifts with respect to the

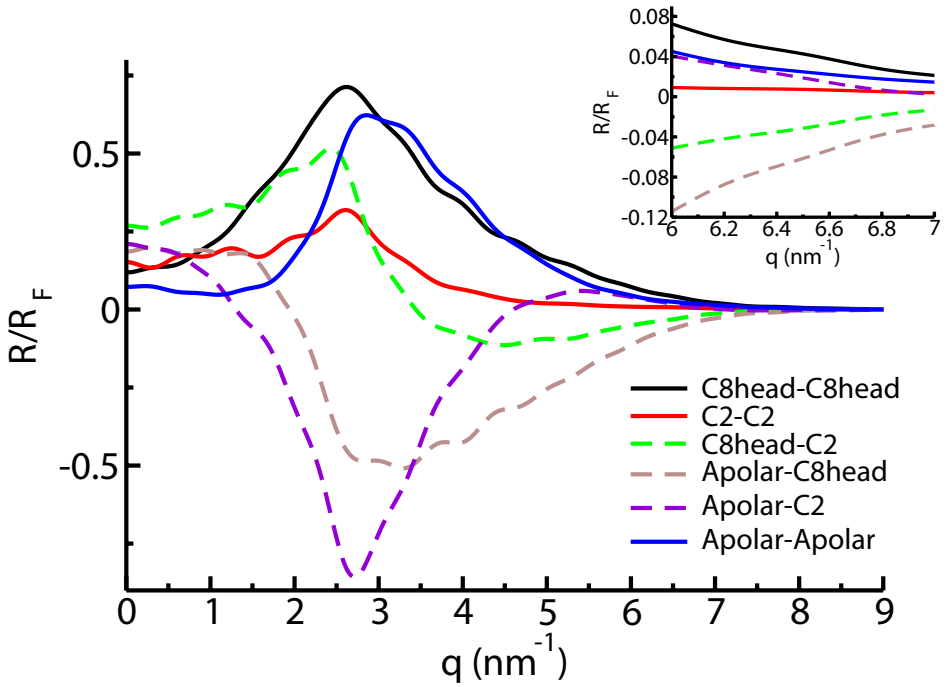

Figure 10: Sub-ionic partitioning of $\frac{R(q)}{R_F(q)}$ highlighting with solid lines self contributions and with dashed lines cross contributions. The self contributions are by construction positive-definite whereas the cross contributions can be either positive or negative depending on the overlap and displacement of real space density profiles of the subspecies. It is from these cross-terms that we can detect real space displacements and mismatches in the distribution of ions. We label C8head as the charged head of both ion types in C[8]-mim$^+$/C[8]-OSO$_3^-$, Apolar as the apolar subcomponents of C[8]-mim$^+$/C[8]-OSO$_3^-$, and C2 as the combination of C[2]-mim$^+$/C[2]-OSO$_3^-$ ions.

interface origin. Figure 11 shows three scenarios in real space and corresponding reciprocal

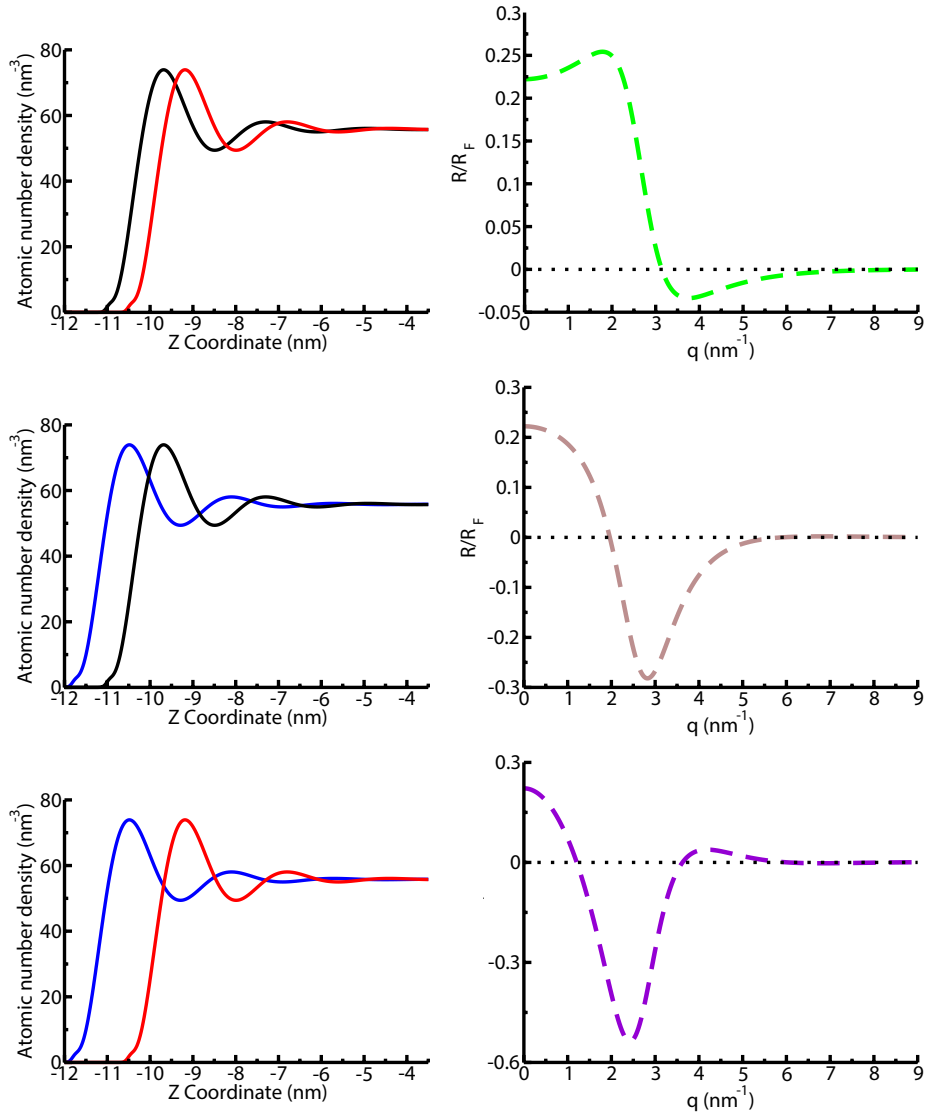

Figure 11: (Left) In real space, three scenarios are depicted where identical idealized density profiles are shifted by different amounts. The color code is defined to match that of the self terms in Fig. 10, blue for the apolar subcomponent, red for charges in the small ions and black for charges in the large ions. (Right) Cross-terms in reciprocal space color-coded to match those in Fig. 10. Green corresponds to the idealized cross-term contribution of large and small ion charges, brown to the idealized cross-term contribution of apolar and large ion charge and purple to the idealized cross-term contribution of apolar and small ion charge to $\frac{R(q)}{R_F(q)}$. These should be contrasted to the very similar cross terms in Fig. 10 resulting from simulation.

space where a simple idealized density profile is shifted by different amounts. These three

scenarios are constructed in analogy to the behavior of cross-terms in Fig. 10. If the shift in the Z direction is zero, then the cross term would be positive definite (like the self terms) and no negative antipeak would be possible. This for example, would be a scenario where large and small ion charges behave identically with no selective preference for the interface. Instead, a small shift, associated with the selective preference for charge of larger ions at the interface when compared to that of the smaller ions results in a positive peak at low q and a negative antipeak at larger q (compare dashed green lines in Figs. 10 and 11).

Larger shifts between two density profiles abolish the low q cross term peak and introduce more prominent negative antipeaks. Such scenarios occur for the charge of both large and small ions when coupled to apolar tails. In the case of the small ions the first peak in the idealized real-space charge distribution is past the first minimum of the apolar distribution (the shift is larger than half a period) and has overlap with the second apolar maximum. This results in a negative antipeak at lower q followed by a positive peak at larger q (compare dashed purple lines in Figs. 10 and 11).

At this point we can begin to interpret the small feature in log scale at around 6.6 nm^{-1} in the inset of Fig. 8(left). This feature results from the complicated interplay of self terms decaying at this q value in Fig. 10 and some of the cross terms increasing, as can be seen from the inset Fig. 10. In particular, the distinct (preferential) behavior of large vs. small ions at the interface has an important role as we see dashed purple and brown curves having opposite slopes at this q value.

4 Conclusions

This study posed the question of whether a mixture of ILs with ions possessing both short and long alkyl tails could be used to form a surface apolar layer that would enclose the more polar subcomponent. The answer to this is yes, and the apolar component is narrow on the order of a single ionic layer. For a very thin film of less than 10 nm, one obtains a highly

structured set of apolar and polar layers that are highly correlated from one interface to the other and no bulk-like liquid in between. For a thicker film in which the width is larger than twice the density decay correlation length away from the interface, clear interfacial and bulk-like regions can be distinguished. At the temperature for this study, the decay of correlations away from the interface occurs at about 6 nm. The first layer is apolar followed by a thicker polar layer (consisting of charges both from long and short ions) and a third apolar bi-layer.

Because the temperature for this study is fairly high and tail lengths are moderate, the normalized reflectivity $\frac{R(q)}{R_F(q)}$ looks like a featureless decaying function of q. Yet, the partition of this function into polar, apolar, positive and negative subcomponents reveals the rich oscillatory nature of the ions at the interface. Further partitioning the normalized reflectivity into the contribution of big and small ionic components reveals complex behavior occurring at larger q values likely impossible to dissect without this type of analysis.

One of the most interesting aspects of this study is that charge alternation which is expected to be mostly a lateral phenomenon can also have a Z-dependent component if the ions have preferential behavior at the interface. How such behavior manifests for other systems, and whether this can be manipulated by electric fields or the nature of solid interfaces is intriguing not only from a scientific perspective but for very practical applications such as tribology. The peaks and antipeaks study of subcomponents of $\frac{R(q)}{R_F(q)}$ opens wide opportunities for analysis of soft matter behavior from the interface all the way deep into the liquid phase.

5 Acknowledgments

This work was supported by NSF Grant No. 1664832 awarded to C.J.M.

6 Supporting Information

Graph showing the time-scale for convergence of atomic density profiles, general derivation of $\frac{R(q)}{R_F(q)}$ in terms of arbitrary disjoint partitions of liquid subcomponents, graph and table with data for fits of polar and apolar density profiles are provided in the Supporting Information free of charge on the ACS Publications website at DOI:XXX

References

(1) Ruiz, V.; Huynh, T.; Sivakkumar, S. R.; Pandolfo, A. G. Ionic Liquid–Solvent Mixtures as Supercapacitor Electrolytes for Extreme Temperature Operation. *RSC Adv.* **2012**, *2*, 5591–5598.

(2) Dagousset, L.; Nguyen, G. T. M.; Vidal, F.; Galindo, C.; Aubert, P.-H. Ionic Liquids and γ-Butyrolactone Mixtures as Electrolytes for Supercapacitors Operating over Extended Temperature Ranges. *RSC Adv.* **2015**, *5*, 13095–13101.

(3) Chagnes, A.; Allouchi, H.; Carré, B.; Lemordant, D. Thermal Analysis of γ-Butyrolactone+ 1 Butyl-3-methyl-imidazolium Ionic Liquids Mixtures. *Solid State Ionics* **2005**, *176*, 1419–1427.

(4) Anouti, M.; Timperman, L. A Pyrrolidinium Nitrate Protic Ionic Liquid-Based Electrolyte for Very Low-Temperature Electrical Double-Layer Capacitors. *Phys. Chem. Chem. Phys.* **2013**, *15*, 6539–6548.

(5) Mellein, B. R.; Aki, S. N. V. K.; Ladewski, R. L.; Brennecke, J. F. Solvatochromic Studies of Ionic Liquid/Organic Mixtures. *J. Phys. Chem. B* **2007**, *111*, 131–138.

(6) Tariq, M.; Shimizu, K.; Esperança, J. M. S. S.; Lopes, J. N. C.; Rebelo, L. P. N. Viscosity Minima in Binary Mixtures of Ionic Liquids + Molecular Solvents. *Phys. Chem. Chem. Phys.* **2015**, *17*, 13480–13494.

(7) Jurado, L. A.; Kim, H.; Arcifa, A.; Rossi, A.; Leal, C.; Spencer, N. D.; Espinosa-Marzal, R. M. Irreversible Structural Change of a Dry Ionic Liquid under Nanoconfinement. *Phys. Chem. Chem. Phys.* **2015**, *17*, 13613–13624.

(8) Anaredy, R. S.; Shaw, S. K. Long-Range Ordering of Ionic Liquid Fluid Films. *Langmuir* **2016**, *32*, 5147–5154.

(9) Smith, A. M.; Lee, A. A.; Perkin, S. The Electrostatic Screening Length in Concentrated Electrolytes Increases with Concentration. *J. Phys. Chem. Lett.* **2016**, *7*, 2157–2163.

(10) Ma, K.; Jarosova, R.; Swain, G. M.; Blanchard, G. J. Charge-Induced Long-Range Order in a Room-Temperature Ionic Liquid. *Langmuir* **2016**, *32*, 9507–9512.

(11) Gebbie, M. A.; Dobbs, H. A.; Valtiner, M.; Israelachvili, J. N. Long-Range Electrostatic Screening in Ionic Liquids. *Proc. Natl. Acad. Sci. U. S. A.* **2015**, *112*, 7432–7437.

(12) Gebbie, M. A.; Smith, A. M.; Dobbs, H. A.; Lee, A. A.; Warr, G. G.; Banquy, X.; Valtiner, M.; Rutland, M. W.; Israelachvili, J. N.; Perkin, S. et al. Long Range Electrostatic Forces in Ionic Liquids. *ChemComm* **2017**, *53*, 1214–1224.

(13) Parr, D.; Chrestenson, J.; Malik, K.; Molter, M.; Zibart, C.; Egan, B.; Haverhals, L. M. Structure and Dynamics at Ionic Liquid/Electrode Interfaces. *ECS Trans.* **2015**, *66*, 35–42.

(14) Robinson, I. K.; Tweet, D. J. Surface X-ray Diffraction. *Rep. Prog. Phys.* **1992**, *55*, 599–651.

(15) Fenter, P.; Cheng, L.; Park, C.; Zhang, Z.; Sturchio, N. Structure of the Orthoclase (001)- and (010)-Water Interfaces by High-Resolution X-ray Reflectivity. *Geochim. Cosmochim. Acta* **2003**, *67*, 4267–4275.

(16) Fenter, P.; Teng, H.; Geissbühler, P.; Hanchar, J.; Nagy, K.; Sturchio, N. Atomic-Scale

Structure of the Orthoclase (001)–Water Interface Measured with High-Resolution X-ray Reflectivity. *Geochim. Cosmochim. Acta* **2000**, *64*, 3663–3673.

(17) Fenter, P. A. X-ray Reflectivity as a Probe of Mineral-Fluid Interfaces: A User Guide. *Rev. Mineral. Geochem.* **2002**, *49*, 149–221.

(18) Lee, S. S.; Park, C.; Fenter, P.; Sturchio, N. C.; Nagy, K. L. Competitive Adsorption of Strontium and Fulvic Acid at the Muscovite–Solution Interface Observed with Resonant Anomalous X-ray Reflectivity. *Geochim. Cosmochim. Acta* **2010**, *74*, 1762–1776.

(19) Schlegel, M. L.; Nagy, K. L.; Fenter, P.; Cheng, L.; Sturchio, N. C.; Jacobsen, S. D. Cation Sorption on the Muscovite (001) Surface in Chloride Solutions using High-Resolution X-ray Reflectivity. *Geochim. Cosmochim. Acta* **2006**, *70*, 3549–3565.

(20) Mezger, M.; Ocko, B. M.; Reichert, H.; Deutsch, M. Surface Layering and Melting in an Ionic Liquid Studied by Resonant Soft X-ray Reflectivity. *Proc. Natl. Acad. Sci. U. S. A.* **2013**, *110*, 3733–3737.

(21) Fukuto, M.; Gang, O.; Alvine, K. J.; Ocko, B. M.; Pershan, P. S. Wetting of Liquid-Crystal Surfaces and Induced Smectic Layering at a Nematic-Liquid Interface: An X-ray Reflectivity Study. *Phys. Rev. E* **2008**, *77*, 031607.

(22) Sloutskin, E.; Ocko, B. M.; Tamam, L.; Kuzmenko, I.; Gog, T.; Deutsch, M. Surface Layering in Ionic Liquids: An X-ray Reflectivity Study. *J. Am. Chem. Soc.* **2005**, *127*, 7796–7804.

(23) Kellogg, G. J.; Pershan, P. S.; Kawamoto, E. H.; Foster, W.; Deutsch, M.; Ocko, B. M. X-ray Reflectivity Measurements and Landau Theory of Smectic Wetting in Liquid Crystal–Benzyl Alcohol Mixtures. *Phys. Rev. E* **1995**, *51*, 4709–4726.

(24) Ocko, B. M.; Wu, X. Z.; Sirota, E. B.; Sinha, S. K.; Deutsch, M. X-ray Reflectivity

Study of Thermal Capillary Waves on Liquid Surfaces. *Phys. Rev. Lett.* **1994**, *72*, 242–245.

(25) Ocko, B. M. Smectic-Layer Growth at Solid Interfaces. *Phys. Rev. Lett.* **1990**, *64*, 2160–2163.

(26) Chu, M. X-ray Reflectivity Study of Ionic Liquids at Electrified Surfaces. Ph.D. thesis, Northwestern University, Evanston, IL, 2017.

(27) Haddad, J.; Pontoni, D.; Murphy, B. M.; Festersen, S.; Runge, B.; Magnussen, O. M.; Steinrück, H.-G.; Reichert, H.; Ocko, B. M.; Deutsch, M. Surface Structure Evolution in a Homologous Series of Ionic Liquids. *Proc. Natl. Acad. Sci. U. S. A.* **2018**, *115*, 1100–1107.

(28) Nishi, N.; Uruga, T.; Tanida, H. Potential Dependent Structure of an Ionic Liquid at Ionic Liquid/Water Interface Probed by X-ray Reflectivity Measurements. *J. Electroanal. Chem.* **2015**, *759*, 129–136.

(29) Rafaja, D.; Fuess, H.; Simek, D.; Kub, J.; Zweck, J.; VacÃ-novÃ¡, J.; Valvoda, V. X-ray Reflectivity of Multilayers with Non-continuous Interfaces. *J. Phys.: Condens. Matter* **2002**, *14*, 5303–5314.

(30) Annapureddy, H. V. R.; Kashyap, H. K.; Biase, P. M. D.; Margulis, C. J. What is the Origin of the Prepeak in the X-ray Scattering of Imidazolium-based Room-Temperature Ionic Liquids? *J. Phys. Chem. B* **2010**, *114*, 16838–16846.

(31) Kashyap, H. K.; Hettige, J. J.; Annapureddy, H. V. R.; Margulis, C. J. SAXS Anti-Peaks Reveal the Length-Scales of Dual Positive–Negative and Polar–Apolar Ordering in Room-Temperature Ionic Liquids. *ChemComm* **2012**, *48*, 5103–5105.

(32) Kashyap, H. K.; Margulis, C. J. (Keynote) Theoretical Deconstruction of the X-ray

Structure Function Exposes Polarity Alternations in Room Temperature Ionic Liquids. *ECS Trans.* **2013**, *50*, 301–307.

(33) Kashyap, H. K.; Santos, C. S.; Daly, R. P.; Hettige, J. J.; Murthy, N. S.; Shirota, H.; Castner, E. W.; Margulis, C. J. How Does the Ionic Liquid Organizational Landscape Change When Nonpolar Cationic Alkyl Groups are Replaced by Polar Isoelectronic Diethers? *J. Phys. Chem. B* **2013**, *117*, 1130–1135.

(34) Kashyap, H. K.; Santos, C. S.; Murthy, N. S.; Hettige, J. J.; Kerr, K.; Ramati, S.; Gwon, J.; Gohdo, M.; Lall-Ramnarine, S. I.; Wishart, J. F. et al. Structure of 1-Alkyl-1-methylpyrrolidinium Bis(trifluoromethylsulfonyl)amide Ionic Liquids with Linear, Branched, and Cyclic Alkyl Groups. *J. Phys. Chem. B* **2013**, *117*, 15328–15337.

(35) Hettige, J. J.; Kashyap, H. K.; Annapureddy, H. V. R.; Margulis, C. J. Anions, the Reporters of Structure in Ionic Liquids. *J. Phys. Chem. Lett.* **2012**, *4*, 105–110.

(36) Hess, B.; Kutzner, C.; van der Spoel, D.; Lindahl, E. GROMACS 4: Algorithms for Highly Efficient, Load-Balanced, and Scalable Molecular Simulation. *J. Chem. Theory Comput.* **2008**, *4*, 435–447.

(37) Van Der Spoel, D.; Lindahl, E.; Hess, B.; Groenhof, G.; Mark, A. E.; Berendsen, H. J. C. GROMACS: Fast, Flexible, and Free. *J. Comput. Chem.* **2005**, *26*, 1701–1718.

(38) Lopes, J. N. C.; Deschamps, J.; Padua, A. A. H. Modeling Ionic Liquids Using a Systematic All-Atom Force Field. *J. Phys. Chem. B* **2004**, *108*, 2038–2047.

(39) Lopes, J. N. C.; Padua, A. A. H.; Shimizu, K. Molecular Force Field for Ionic Liquids IV: Trialkylimidazolium and Alkoxycarbonyl-Imidazolium Cations; Alkylsulfonate and Alkylsulfate Anions. *J. Phys. Chem. B* **2008**, *112*, 5039–5046.

(40) Jorgensen, W. L.; Maxwell, D. S.; Tirado-Rives, J. Development and Testing of the

OPLS All-Atom Force Field on Conformational Energetics and Properties of Organic Liquids. *J. Am. Chem. Soc.* **1996**, *118*, 11225–11236.

(41) Mcdonald, N. A.; Jorgensen, W. L. Development of an All-Atom Force Field for Heterocycles. Properties of Liquid Pyrrole, Furan, Diazoles, and Oxazoles. *J. Phys. Chem. B* **1998**, *102*, 8049–8059.

(42) Price, M. L. P.; Ostrovsky, D.; Jorgensen, W. L. Gas-Phase and Liquid-State Properties of Esters, Nitriles, and Nitro Compounds with the OPLS-AA Force Field. *J. Comput. Chem.* **2001**, *22*, 1340–1352.

(43) García-Garabal, S.; Vila, J.; Rilo, E.; Domínguez-Pérez, M.; Segade, L.; Tojo, E.; Verdía, P.; Varela, L.; Cabeza, O. Transport Properties for 1-Ethyl-3-methylimidazolium n-Alkyl Sulfates: Possible Evidence of Grotthuss Mechanism. *Electrochim. Acta* **2017**, *231*, 94–102.

(44) Macchiagodena, M.; Ramondo, F.; Triolo, A.; Gontrani, L.; Caminiti, R. Liquid Structure of 1-Ethyl-3-methylimidazolium Alkyl Sulfates by X-ray Scattering and Molecular Dynamics. *J. Phys. Chem. B* **2012**, *116*, 13448–13458.

(45) Bussi, G.; Donadio, D.; Parrinello, M. Canonical Sampling Through Velocity Rescaling. *J. Chem. Phys.* **2007**, *126*, 014101.

(46) Berendsen, H. J. C.; Postma, J. P. M.; van Gunsteren, W. F.; DiNola, A.; Haak, J. R. Molecular Dynamics with Coupling to an External Bath. *J. Chem. Phys.* **1984**, *81*, 3684–3690.

(47) Nosé, S. A Unified Formulation of the Constant Temperature Molecular Dynamics Methods. *J. Chem. Phys.* **1984**, *81*, 511–519.

(48) Nose, S. A Molecular Dynamics Method for Simulations in the Canonical Ensemble. *Mol. Phys.* **1984**, *52*, 255–268.

(49) Parrinello, M.; Rahman, A. Polymorphic Transitions in Single Crystals: A New Molecular Dynamics Method. *J. Appl. Phys.* **1981**, *52*, 7182–7190.

(50) Hockney, R.; Goel, S.; Eastwood, J. Quiet High-Resolution Computer Models of a Plasma. *J. Comput. Phys.* **1974**, *14*, 148–158.

(51) Darden, T.; York, D.; Pedersen, L. Particle Mesh Ewald: An N log(N) Method for Ewald Sums in Large Systems. *J. Chem. Phys.* **1993**, *98*, 10089–10092.

(52) Essmann, U.; Perera, L.; Berkowitz, M. L.; Darden, T.; Lee, H.; Pedersen, L. G. A Smooth Particle Mesh Ewald Method. *J. Chem. Phys.* **1995**, *103*, 8577–8593.

(53) Yeh, I.-C.; Berkowitz, M. L. Ewald Summation for Systems with Slab Geometry. *J. Chem. Phys.* **1999**, *111*, 3155–3162.

(54) Yeh, I.-C.; Wallqvist, A. On the Proper Calculation of Electrostatic Interactions in Solid-Supported Bilayer Systems. *J. Chem. Phys.* **2011**, *134*, 055109.

(55) Fenter, P.; Lee, S. S.; Skelton, A. A.; Cummings, P. T. Direct and Quantitative Comparison of Pixelated Density Profiles with High-Resolution X-ray Reflectivity Data. *J. Synchrotron Radiat.* **2010**, *18*, 257–265.

(56) Fenter, P.; Kerisit, S.; Raiteri, P.; Gale, J. D. Is the Calcite–Water Interface Understood? Direct Comparisons of Molecular Dynamics Simulations with Specular X-ray Reflectivity Data. *J. Phys. Chem. C* **2013**, *117*, 5028–5042.

(57) Park, C.; Fenter, P.; Zhang, Z.; Cheng, L.; Sturchio, N. C. Structure of The Fluorapatite (100)-Water Interface by High-Resolution X-ray Reflectivity. *Am. Mineral.* **2004**, *89*, 1647–1654.

(58) Zimmermann, K.-M.; Tolan, M.; Weber, R.; Stettner, J.; Doerr, A. K.; Press, W. Phase Determination of X-ray Reflection Coefficients. *Phys. Rev. B* **2000**, *62*, 10377–10382.

(59) Prakash, A.; Pfaendtner, J.; Chun, J.; Mundy, C. J. Quantifying the Molecular-Scale Aqueous Response to the Mica Surface. *J. Phys. Chem. C* **2017**, *121*, 18496–18504.

(60) Steinrück, H.-G.; Cao, C.; Tsao, Y.; Takacs, C. J.; Konovalov, O.; Vatamanu, J.; Borodin, O.; Toney, M. F. The Nanoscale Structure of the Electrolyte–Metal Oxide Interface. *Energy Environ. Sci.* **2018**, *11*, 594–602.

(61) Als-Nielsen, J.; McMorrow, D. *Elements of Modern X-ray Physics*; John Wiley & Sons, Inc.: New York, 2011.

(62) Sloutskin, E.; Lynden-Bell, R. M.; Balasubramanian, S.; Deutsch, M. The Surface Structure of Ionic Liquids: Comparing Simulations with X-ray Measurements. *J. Chem. Phys.* **2006**, *125*, 174715.

(63) Regan, M. J.; Pershan, P. S.; Magnussen, O. M.; Ocko, B. M.; Deutsch, M.; Berman, L. E. X-ray Reflectivity Studies of Liquid Metal and Alloy Surfaces. *Phys. Rev. B* **1997**, *55*, 15874–15884.

(64) Sun, X.; Dang, L. X. Computational Studies of Aqueous Interfaces of RbBr Salt Solutions. *J. Chem. Phys.* **2009**, *130*, 124709.

(65) Mars, J.; Hou, B.; Weiss, H.; Li, H.; Konovalov, O.; Festersen, S.; Murphy, B. M.; Rütt, U.; Bier, M.; Mezger, M. Surface Induced Smectic Order in Ionic Liquids-an X-ray Reflectivity Study of $[C_{22}C_1\text{im}]^+[\text{NTf}_2]^-$. *Phys. Chem. Chem. Phys.* **2017**, *19*, 26651–26661.

(66) Araque, J. C.; Hettige, J. J.; Margulis, C. J. Modern Room Temperature Ionic Liquids, a Simple Guide to Understanding Their Structure and How It May Relate to Dynamics. *J. Phys. Chem. B* **2015**, *119*, 12727–12740.

(67) Santos, C. S.; Annapureddy, H. V. R.; Murthy, N. S.; Kashyap, H. K.; Castner, E. W.; Margulis, C. J. Temperature-Dependent Structure of Methyltributylammonium Bis(tri-

fluoromethylsulfonyl)amide: X Ray Scattering and Simulations. *J. Chem. Phys.* **2011**, *134*, 064501.

(68) Hettige, J. J.; Kashyap, H. K.; Margulis, C. J. Communication: Anomalous Temperature Dependence of the Intermediate Range Order in Phosphonium Ionic Liquids. *J. Chem. Phys.* **2014**, *140*, 111102.

(69) Bruce, D. W.; Cabry, C. P.; Lopes, J. N. C.; Costen, M. L.; D'Andrea, L.; Grillo, I.; Marshall, B. C.; McKendrick, K. G.; Minton, T. K.; Purcell, S. M. et al. Nanosegregation and Structuring in the Bulk and at the Surface of Ionic-Liquid Mixtures. *J. Phys. Chem. B* **2017**, *121*, 6002–6020.

(70) Qin, L.; Wang, X.-H. Surface Adsorption and Thermodynamic Properties of Mixed System of Ionic Liquid Surfactants with Cetyltrimethyl Ammonium Bromide. *RSC Adv.* **2017**, *7*, 51426–51435.

TOC Graphic